Field-driven spin structure evolution in $MnCr_2S_4$: A high-field single-crystal neutron diffraction study

F. Duc,[1] N. Qureshi,[2] H. Suwa,[3] E. Ressouche,[4] M. Songvilay,[5] O. Prokhnenko,[6] A. Gazizulina,[6] F. Bourdarot,[4] V. Tsurkan,[7,8] S. Zherlitsyn,[9] L. Prodan,[7,8] A. Bertin,[10,11] A. Schneidewind,[12] A. Hoser,[6] M. Uhlarz,[9] T. Herrmannsdörfer,[9] J. Wosnitza,[9,10] V. Simonet,[5] and S. Chattopadhyay[9,13,*]

[1]*CNRS, Laboratoire National des Champs Magnétiques Intenses, Université Grenoble Alpes, Université Toulouse 3, INSA Toulouse, EMFL, 31400 Toulouse, France*

[2]*Institut Laue-Langevin, 71 avenue des Martyrs, CS20156, 38042 Grenoble Cédex 9, France*

[3]*Department of Physics, The University of Tokyo, Tokyo 113-0033, Japan*

[4]*Université Grenoble Alpes, CEA, IRIG, MEM, MDN, 38000 Grenoble, France*

[5]*Université Grenoble Alpes, CNRS, Institut Néel, 38000 Grenoble, France*

[6]*Helmholtz-Zentrum Berlin für Materialien und Energie, 14109 Berlin, Germany*

[7]*Experimental Physics V, Center for Electronic Correlations and Magnetism, Institute of Physics, University of Augsburg, D-86159 Augsburg, Germany*

[8]*Institute of Applied Physics, Moldova State University, MD 2028 Chisinau, Republic of Moldova*

[9]*Hochfeld-Magnetlabor Dresden (HLD-EMFL) and Würzburg-Dresden Cluster of Excellence ct.qmat, Helmholtz-Zentrum Dresden-Rossendorf, 01328 Dresden, Germany*

[10]*Institut für Festkörper- und Materialphysik, Technische Universität Dresden, 01062 Dresden, Germany*

[11]*II. Physikalisches Institut, Universität zu Köln, Zülpicher Str. 77, 50937 Köln, Germany*

[12]*Jülich Centre for Neutron Science (JCNS) at Heinz Maier-Leibnitz Zentrum (MLZ), Forschungszentrum Jülich GmbH, Lichtenbergstraße 1, 85748 Garching, Germany*

[13]*UGC-DAE Consortium for Scientific Research Mumbai Centre, 246-C CFB, BARC Campus, Mumbai 400085, India*

(Received 28 August 2024; revised 8 November 2024; accepted 8 November 2024; published 9 December 2024)

We present a comprehensive microscopic insight into the spin configurations within the bond-frustrated cubic spinel compound $MnCr_2S_4$ directly unveiled through extensive single-crystal neutron diffraction studies carried out in zero magnetic field and in fields up to 35 T. While our zero field results confirm the ferrimagnetic structure with an antiparallel arrangement of the magnetic Cr^{3+} and Mn^{2+} sublattices below $T_{FiM} \approx 65$ K, as well as the presence of the exotic Yafet-Kittel phase below $T_{YK} \approx 5$ K, our data measured in fields enable us to precisely determine the field-induced magnetic structures and their evolution across the phase transitions at $\mu_0 H_1 \approx 11$ T and $\mu_0 H_2 \approx 25$ T and beyond that towards $\mu_0 H_3$ ($\approx$50 T). Additionally, combining our experimental findings with mean-field-theory calculations reveals a complex field dependence of the Mn-Mn and Mn-Cr exchange interactions across the different phases, highlighting the significant influence of spin-lattice coupling in this material.

DOI: 10.1103/PhysRevB.110.214416

I. INTRODUCTION

Magnetic frustration lies at the core of many exotic and unconventional magnetic phenomena, providing a rich landscape for the exploration of novel magnetism and associated effects [1–3]. The family of frustrated spinel compounds, characterized by the general formula AB_2X_4, where either A, B, or both sites are magnetic (with X = O, S, Se), stands out as an exceptional resource for realizing a diverse range of such phenomena. These include manifestations such as spin-orbital liquids, spiral spin-liquids, spin-driven multiferroicity, and spin-Peierls-like phases [4–7].

Spinel materials, where both A and B sites are magnetic, offer a unique opportunity to investigate the combined effects of geometric and bond frustrations. The geometric aspect arises from the pyrochlore-type B sublattice with antiferromagnetic exchange coupling J_{BB}. Notably, a pyrochlore-type spin arrangement can induce significant frustration in three dimensions [8,9]. In spinels with magnetic B sites, there can also be competition with further-neighbor interactions [10,11]. On the other hand, the A sublattice forms a bipartite diamond structure and contributes to bond frustration through competing antiferromagnetic J_{AA} and J_{AB} interactions.

In this paper, our focus is on $MnCr_2S_4$, a magnetically frustrated cubic spinel system (space group $Fd\bar{3}m$), in which the two magnetic ions, viz., Mn^{2+} ($S = \frac{5}{2}$) and Cr^{3+} ($S = \frac{3}{2}$) occupy the A (tetrahedral) and B (octahedral) site, respectively, as illustrated in Fig. 1(a) (also see the Supplemental Material [12]). In absence of any external magnetic field, $MnCr_2S_4$ undergoes two magnetic phase transitions: the first one, at $T_{FiM} \approx 65$ K, corresponds to a paramagnetic (PM) to ferrimagnetic (FiM) transition with antiparallel Mn^{2+} and Cr^{3+} spins, while the second one appears at $T_{YK} \approx 5$ K and was proposed to be a Yafet-Kittel (YK) phase [13–20]. The YK

*Contact author: sumanta@csr.res.in

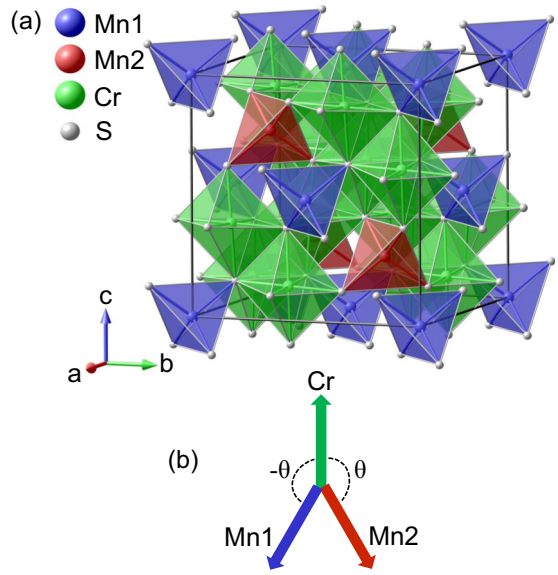

FIG. 1. (a) Perspective view of the crystal structure of $MnCr_2S_4$. (b) Illustration of the spin configuration in the Yafet-Kittel phase, where the two crystallographically equivalent Mn sites are depicted using distinct colors (Mn1 and Mn2) to differentiate them, as their field-induced spin configurations become nonequivalent.

phase emerges when J_{AA} and J_{AB} exhibit comparable strength. This magnetic structure results in a symmetric canted-spin arrangement, where Mn1 and Mn2 moments form angles of $+\theta$ and $-\theta$ with the Cr moment, respectively [Fig. 1(b)]. Multiferroic properties were reported recently in $MnCr_2S_4$, for both YK and FiM phases [21,22].

This compound exhibits an even more intricate behavior when subjected to a high magnetic field, as evidenced by its remarkably diverse magnetic phase diagram [23–25], which at low temperatures reveals five field-induced phase transitions occurring at $\mu_0 H_1 \approx 11\,\mathrm{T}$, $\mu_0 H_2 \approx 25\,\mathrm{T}$, $\mu_0 H_3 \approx 50\,\mathrm{T}$, $\mu_0 H_4 \approx 75\,\mathrm{T}$, and $\mu_0 H_5 \approx 85\,\mathrm{T}$, with a particularly robust magnetization-plateau state of $6\,\mu_B$/f.u. for fields between 25 and 50 T. Extensive theoretical and experimental efforts have been devoted to identifying the microscopic driving forces behind these phenomena [17,18,26]. Drawing on analogies with the quantum-lattice gas models [27,28], Tsurkan *et al.* argued that the YK and the field-induced phases below and above the magnetization plateau represent exotic spin-superfluid and supersolid states, respectively [24].

Subsequent investigations, using dielectric and pyrocurrent measurements up to 60 T, provided the support for spin-driven multiferroicity in these specific states [21]. High-field magnetostriction and ultrasound measurements, as well as observations of the magnetization-plateau phase and multiferroic properties, confirm the presence of strong spin-lattice coupling between Mn and Cr spins in $MnCr_2S_4$. The latter was included, via a biquadratic exchange term, in a classical Monte Carlo calculation-based model to explain the high-field magnetization, magnetostriction, and sound-velocity results. This model estimated J_{MnMn} (AF) $\approx$ J_{MnCr} (AF) and J_{CrCr} to be ferromagnetic (F) indicating a favorable condition for the YK phase stabilization in $MnCr_2S_4$, in agreement with previous estimates [15,24], and provided predictions regarding the probable spin structures of the successive field-induced phases [25]. More recently, their microscopic nature has been investigated using soft x-ray absorption spectroscopy (XAS) and magnetic circular dichroism (XMCD) in pulsed magnetic fields up to 40 T [29]. It is noteworthy that Mn XAS and XMCD only provide average information on the two nonequivalent Mn sublattices in the field-induced phases. Combined with high-field ultrasound and macroscopic thermodynamic measurements, this study revealed the presence of a tetracritical point in the H-T phase diagram at $\sim$10 K around 12 T. This point has been suggested to be the convergence of FiM, YK, low-field asymmetric, and plateau states. Considering $MnCr_2S_4$ as a conventional Heisenberg system, the existence of such a tetracritical point is rather exceptional [30].

In this study, we present a comprehensive investigation employing both powder neutron diffraction (PND) and single-crystal neutron diffraction (SCND) to determine the magnetic structures of $MnCr_2S_4$. This study extends up to 35 T and involves the use of various instruments across different neutron facilities. Previous examinations of this compound were limited to PND studies solely at zero field (ZF) [16,19,31,32]. Although the existence of a YK phase was anticipated, the low-resolution and overlapping reflections inherent in powder data led to conflicting outcomes. Moreover, direct evidence of field-induced magnetic structures has been lacking thus far. Consequently, there was a pressing need for SCND to definitively verify the predicted magnetic structures. By combining our experimental results with the mean-field approximation of the spin Hamiltonian, we estimate the exchange couplings and their field dependencies, providing further insights into the magnetic behavior of $MnCr_2S_4$.

II. EXPERIMENTAL DETAILS

Polycrystalline samples of $MnCr_2S_4$ were prepared by solid-state reactions. Stoichiometric quantities of high-purity Cr (99.99%), Mn (99.995%), and S (99.999%) powders were mixed and ground thoroughly. The mixture was then pressed into pellets and put into a quartz ampule evacuated to 10^{-2} mbar, sealed, and heated at 900 °C for one week. This sintering process was repeated thrice to produce a single-phase material. High-quality $MnCr_2S_4$ single crystals were grown by chemical transport reactions from the ternary polycrystalline material, as described in Refs. [20,33]. For the present neutron-diffraction study, crystals were from the same batch as the one previously used for high-field magnetization and ultrasound measurements [24]. All of them had irregular shapes of roughly similar dimensions ($\sim 2.5 \times 2.5 \times 2\,\mathrm{mm}^3$).

PND experiments were carried out in ZF between 2 and 80 K on the E6 diffractometer at BER II neutron scattering facility of the Helmholtz-Zentrum Berlin (HZB) using a wavelength of $\lambda = 2.45$ Å.

SCND studies were performed on the thermal neutron single-crystal two-axis diffractometer D23 and on the IN22 spectrometer (both CEA-CRG) at the Institut Laue Langevin (Grenoble, France) as well as on the HFM/EXED instrument [34–36] at the HZB. On D23, data were collected at several temperatures between 1.6 and 80 K in ZF and dc fields up to 6 T on a single crystal of $MnCr_2S_4$ mounted inside a 6-T

vertical cryomagnet. The sample was previously aligned on the OrientExpress neutron Laue diffractometer so that the field was applied along the [111] direction. The D23 diffractometer was equipped with a lifting-arm detector and operated in normal-beam mode with an incident wavelength $\lambda = 1.274$ Å selected from a Cu(200) monochromator.

To further probe the field-driven evolution of the magnetic structure, especially across $\mu_0 H_1$ (≈11 T) and in between $\mu_0 H_1$ and $\mu_0 H_2$ (≈25 T), complementary measurements were performed on the Extreme Environment Diffractometer (EXED) within the High Field Magnet (HFM) facility at the HZB. This instrument combined a horizontal-field dc hybrid magnet (HFM) capable of reaching fields up to 26 T and a time-of-flight neutron diffractometer (EXED) [34–37]. The sample was mounted in a ^{4}He-flow cryostat equipped with a rotation stage around the vertical axis with an angular range of 180°, allowing the sample orientation to be adjusted *in situ*. The sample was aligned with the [111] direction along the field and the [$\bar{1}$10] axis lying in the horizontal scattering plane and perpendicular to the field. Working in diffraction mode, we measured the field dependence at 2 and 12 K of the reflections (0$\bar{2}$0) and (2$\bar{2}$0), as well as the field dependence at 2 K of the reflection (1$\bar{3}$1). A rotation of 37.5° and 11° around the vertical axis was applied to reach the magnetic reflections (0$\bar{2}$0) and (1$\bar{3}$1), respectively. Data reduction was done using the Mantid software [38], which takes into account the vanadium normalization as well as the Lorentz correction.

An additional experiment was carried out on the IN22 spectrometer, operated in the double-axis mode (without analyzer) and equipped with a pulsed-field set-up, including a 1.15-MJ generator and a 40-T horizontal-field cryomagnet having a field-pulse duration of ∼100 ms [39]. In this magnet, the constraints of the sample holder require the sample to be affixed to one of its faces, with one edge of the crystal aligned parallel to the direction of the applied field. This limitation restricted our abilities to measure with the same field alignment as for the lower field experiments. Because of the irregular shapes of our $MnCr_2S_4$ single crystals, which have (111)-type faces with edges oriented along ⟨110⟩ directions, the field was applied along the [110] direction, with the scattering plane defined by [110] and [001]. We note that applying the field along [110] is not essentially different from applying it along [111], in terms of the magnetic behavior of $MnCr_2S_4$. Given the weak single-ion anisotropy of Mn^{2+} and Cr^{3+}, this compound shows rather similar field dependencies in these two field orientations, especially in the high-field regime, as reported in Refs. [20,25,29]. With that mounting, we were able to measure the (002) reflection. Measurements were performed in fields up to 35 T at several temperatures between 2 and 18 K, using a wavelength of 1.208 Å.

All single-crystal data were analyzed using MAG2POL [40], while FULLPROF Suite package [41] was used for the Rietveld analysis of powder data.

III. RESULTS, ANALYSES, AND DISCUSSION

A. Neutron diffraction in zero field

The ZF experiments aimed at reinvestigating more closely the magnetic structures, together with the nuclear one, above and below the ordering temperatures. Special attention was paid to the temperature dependence of certain characteristic Bragg positions, where magnetic signal is expected, particularly at the transition to the YK phase, as reported in Refs. [16,19]. PND and SCND data measured in ZF at 80 K were used as reference data to determine crystallographic and instrumental parameters. Theses parameters were subsequently fixed to refine the magnetic structures below $T_{FiM} = 65$ K. The propagation vector $\mathbf{k} = (0,0,0)$ describing the periodicity of the magnetic phases was derived from PND patterns recorded across the entire temperature range from 2 K to T_{FiM}. Figure 2 displays a typical PND pattern of $MnCr_2S_4$ collected at ZF for $T = 10$ K. Refinement of the magnetic structure from this data revealed a ferrimagnetic structure with an antiparallel arrangement of Cr and Mn sublattices along ⟨111⟩, in agreement with previous PND results [16,19,31,32]. The broad feature between 35° and 45° was systematically observed throughout the measured temperature range, up to 80 K. As it does not vary with temperature, it was attributed to the sample environment rather than to any intrinsic properties of the sample itself. Upon further temperature reduction below T_{YK}, we note a slight increase in the intensities of the peaks, although the emergence of characteristic reflections such as {200}, {420}, and {311} remains undetected. The presence of these reflections would typically indicate the opening of a canting angle between Mn1 and Mn2 moments.

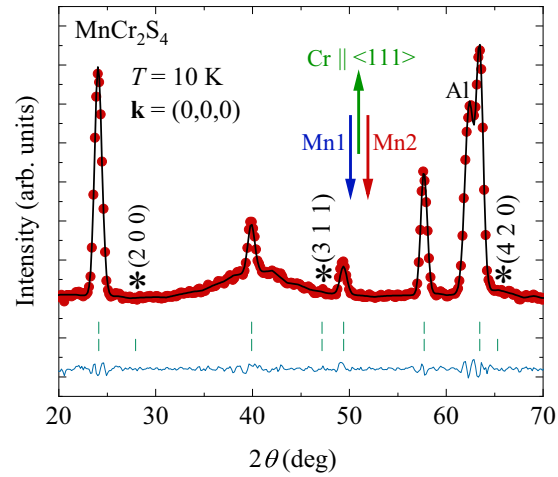

FIG. 2. Typical powder neutron diffraction (10 K, 0 T) pattern of $MnCr_2S_4$ along with Rietveld refinement of the nuclear and magnetic structures (E6, HZB). Red circles, black, and blue lines correspond to the measured, fitted, and difference between the measured and fitted intensities, respectively. The upper and lower vertical bars in green denote positions of the nuclear and the magnetic Bragg reflections, respectively. The positions of the characteristic (200), (311), and (420) reflections, expected to emerge in the YK phase, are indicated with the asterisk signs. A peak from aluminium background is also indicated. A sketch of the antiparallel alignment of Cr and Mn moments along ⟨111⟩, obtained by refinement, is shown above the powder pattern.

1. Temperature dependence of characteristic reflections

In order to further investigate this matter and gather additional information regarding the ZF magnetic structure below T_{YK}, we followed the temperature dependence of ten

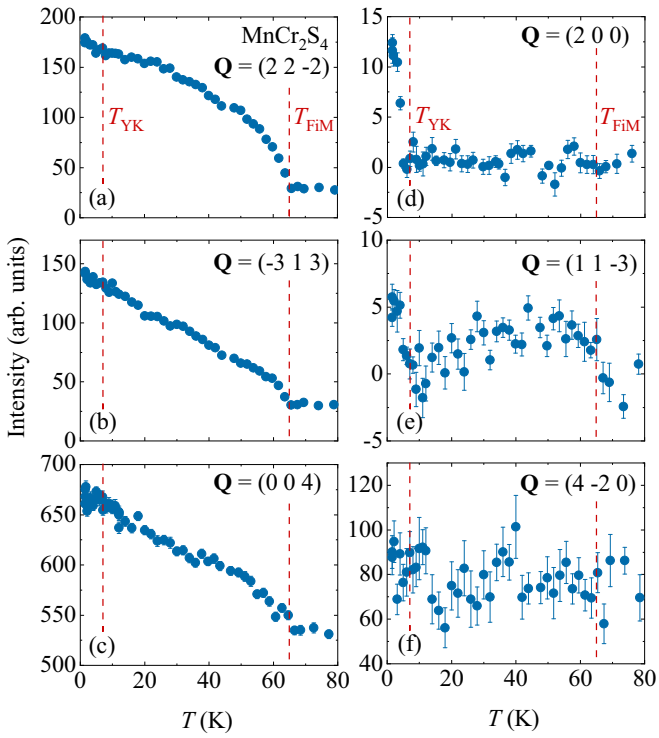

FIG. 3. Neutron counts at the peak maximum as a function of temperature for six types of Bragg reflections extracted from the zero-field single-crystal neutron-diffraction measurements (D23, CEA-CRG, ILL).

nonequivalent reflections between 80 and 1.6 K by SCND. Compared to PND, SCND allows for the collection of more precise data, albeit requiring consideration of magnetic domains resulting from lattice symmetry. Figures 3(a)–3(f) illustrate the temperature dependencies of six of these characteristic Bragg reflections (see Fig. S1 within the Supplemental Material [12] for other reflections), providing a comprehensive insight into their thermal evolution:

(I) Certain reflections such as $(22\bar{2})$, $(\bar{3}13)$, and (004) begin to increase below T_{FiM}, showing a gradual rise in intensity with decreasing temperature. However, a closer examination reveals variations in their temperature dependence owing to differing sensitivities to the Cr moment (the order parameter) and the Mn longitudinal moment, which is polarized by the Cr moment. In particular, an anomaly below T_{YK} is evident in $(22\bar{2})$, indicating the sensitivity to the transverse component of the Mn moment.

(II) Two reflections, namely (200) and $(11\bar{3})$, although faint, become discernible and exhibit sensitivity to the YK magnetic structure, demonstrating a sharp increase in intensity as temperature decreases below T_{YK}. Hence, these reflections are also responsive to the transverse component of the Mn moment. On the other hand, they do not exhibit significant features around T_{FiM}. The low intensity of the (200) reflection in ZF conditions likely accounts for its absence in our PND data and those of Refs. [31,32]. Nonetheless, the rising intensity below T_{YK} [applicable to both (200) and $(11\bar{3})$] suggests emerging canting between the Mn1 and Mn2 moments, a topic we will explore further in our discussion on ZF magnetic structure determination.

(III) In contrast to findings by Plumier *et al.* [19], within our estimated error limits, the reflection $(4\bar{2}0)$, shown in Fig. 3(f), persists across the entire measured temperature range, exhibiting practically temperature-independent behavior insensitive to both transitions.

2. The zero-field magnetic structure at 12 K: The FiM state

The nuclear-structure refinement was carried out at T = 80 K (space group $Fd\bar{3}m$, origin choice 1) using a SCND dataset consisting of 232 Bragg reflections. The atomic positions, the isotropic temperature factors, the diagonal elements of the extinction-correction tensor within an empirical SHELX-like model [42], along with an overall scale factor were initially refined and then held constant for subsequent magnetic-structure analysis. The resulting parameters are shown in Table S1 within the Supplemental Material [12].

To determine the magnetic structure at 12 K, i.e., in the FiM regime, the data reduction option of MAG2POL was used to calculate, in $P1$ symmetry, the difference between the raw data collected at 12 and 80 K. This approach prevents the averaging of the different magnetic domains, thereby generating a dataset comprising purely magnetic intensities. All reflections with negative intensity or with suspiciously large error bars, as well as the {400} reflections were removed from the resulting dataset. The latter are the strongest nuclear reflections and could lead to artifacts in the intensities based on the difference calculation. The {200} and {113} reflections were kept at 12 K (even if their intensity was 0) to have the same set of reflections as at 1.6 K (this led to a dataset of 96 reflections for the refinements of the magnetic structures). We described the coplanar magnetic structures in a plane made by the basis vectors $[1\bar{1}\bar{1}]\sqrt{3}$ and $[110]/\sqrt{2}$ compatible with the $Fd\bar{3}m$ space group and $\mathbf{k}$ = (0,0,0), already depicted in Ref. [21]. Extinction parameters were initially constrained to $x_{11} = x_{22} = x_{33}$ and then fixed to refined values. Since the magnetic moments are supposed to be aligned along the ⟨111⟩ directions, four magnetic domains corresponding to the four threefold rotation axes in the cubic lattice were considered. The symmetry operators relating the different magnetic domains are

(1) x y z
(2) –x –y+1/2 z+1/2
(3) –x+1/2 y+1/2 –z
(4) x+1/2 –y –z+1/2

where (2) to (4) correspond to the three twofold axes along the ⟨100⟩ cubic directions within the (0 0 0)+ set of space group $Fd\bar{3}m$. The refinement confirms an FiM arrangement yielding 3.75(3) μ_B along the ⟨111⟩ direction on the Mn and 2.59(2) μ_B on Cr (R_F = 10.8%). Figure 4 shows the corresponding I_{obs} versus I_{cal} plot obtained from our fit. Whereas domains are expected to be equally populated, the refinement of domain populations led to 0.23, 0.34(1), 0.22(1), 0.21(2), where the first population is calculated as one minus the sum of the rest. The four domains are shown in Fig. 5.

3. The zero-field magnetic structure at 1.6 K: The YK phase

We followed the same procedure as described above to generate purely magnetic intensities and to remove suspicious reflections from the reflection list. Notably, the reflection lists

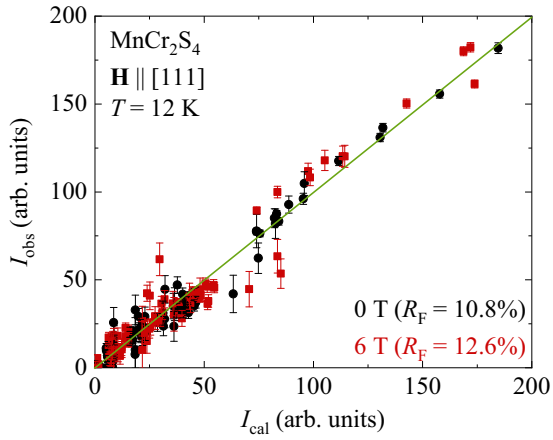

FIG. 4. Observed vs calculated intensity plot for 0 and 6 T data measured at 12 K (D23, CEA-CRG, ILL).

used for the 1.6 and 12 K refinements are identical. This consistency is crucial for validating any potential disparities in the magnetic structures between these two temperatures. However, at this instance, a second coefficient was refined for the Mn spins to account for canting, which we assumed to be along [110] for the Mn1 spins and along $[\bar{1}\bar{1}0]$ for the Mn2 spins. When the magnetic moments deviate from each of the ⟨111⟩ directions, each of the four magnetic domains splits into another three, related by the threefold rotation operator. In this case, the twelve symmetry operators relating the magnetic domains are:

(1) x y z
(2) z x y
(3) y z x
(4) –x –y+1/2 z+1/2
(5) z+1/2 –x –y+1/2
(6) –y+1/2 z+1/2 –x
(7) –x+1/2 y+1/2 –z
(8) –z –x+1/2 y+1/2
(9) y+1/2 –z –x+1/2
(10) x+1/2 –y –z+1/2
(11) –z+1/2 x+1/2 –y
(12) –y –z+1/2 x+1/2

To understand the relationship between the domains, the twelve domains are displayed with exaggerated canting in Fig. 6. For each domain the view is along the Cr-spin direction. Note that in the three domains of each row, the canting direction is connected by a three-fold rotation axis. For instance, domains (1), (6), and (8) are related, as are domains

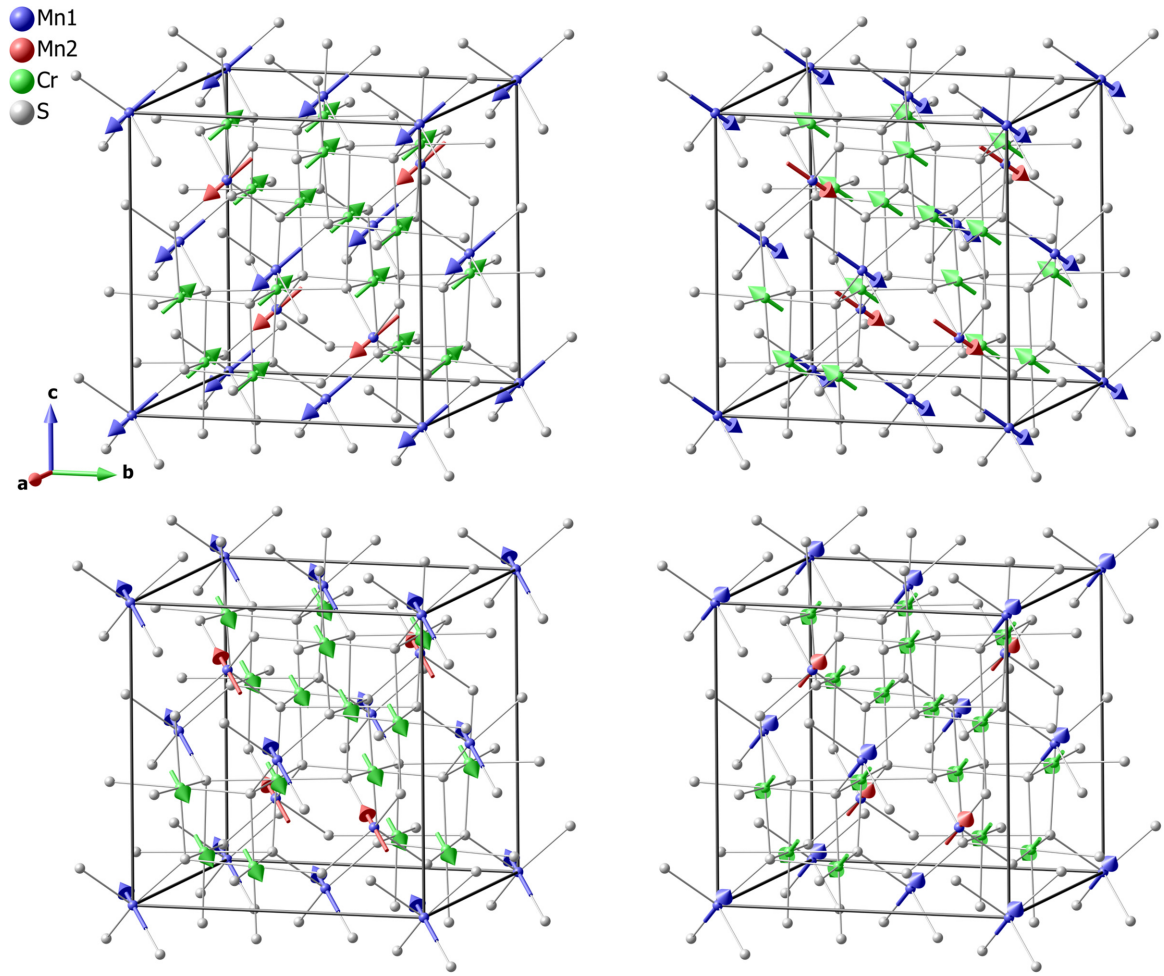

FIG. 5. Ferrimagnetic spin configuration at 12 K, showing antiparallel alignment of the Cr and Mn spins along ⟨111⟩, in the four possible magnetic domain orientations corresponding to the four threefold rotation axes in the cubic lattice of $MnCr_2S_4$.

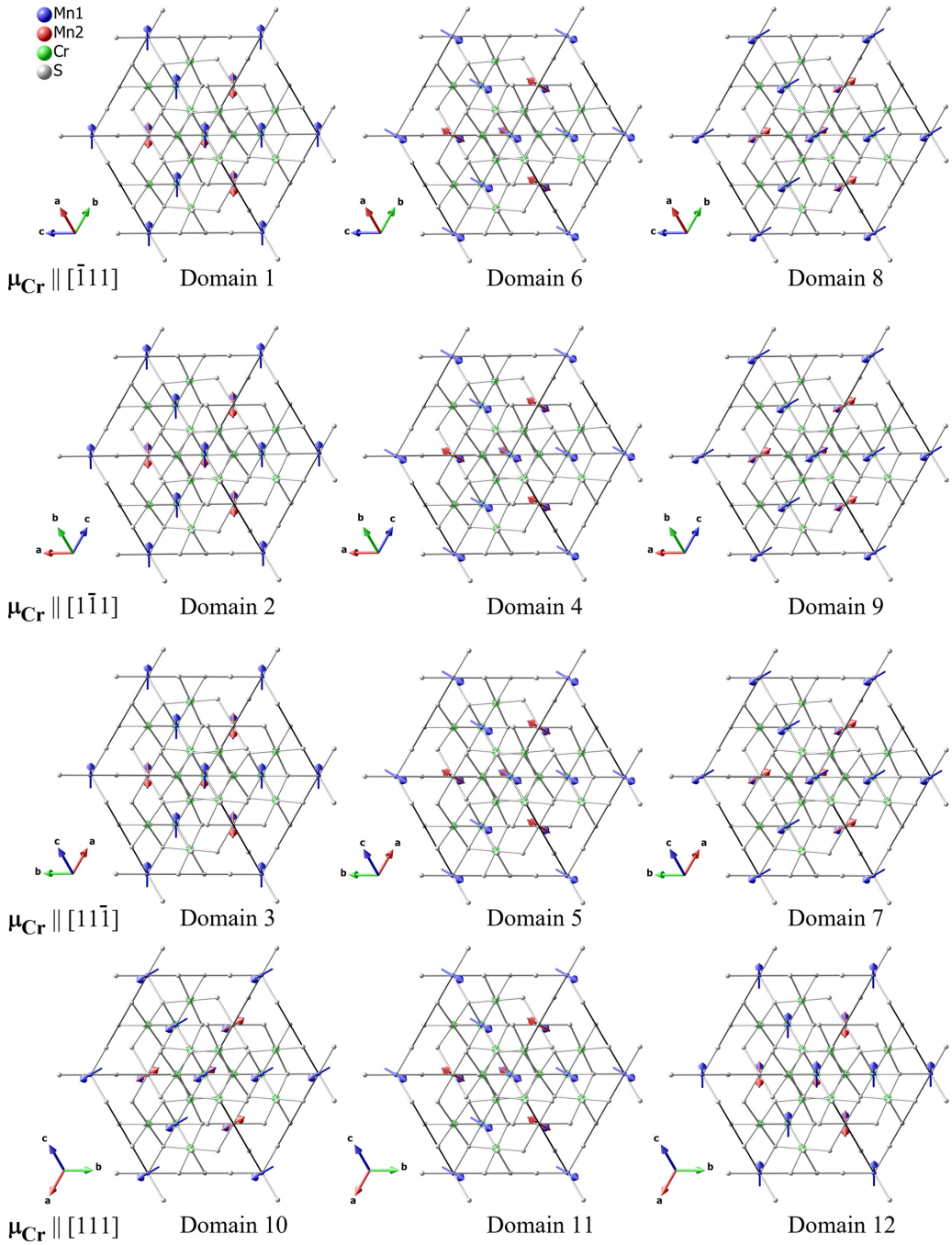

FIG. 6. Overview of the twelve magnetic domains at 1.6 K. For each domain the view is along the Cr-spin direction. In each row, the canting direction within the three domains is related by a threefold rotation axis.

(2), (4), and (9). Consequently, the refined population at 12 K was evenly distributed among these newly balanced domains. For example, the population of domain (1) at 12 K is 0.23, resulting in domains (1), (6), and (8) at 1.6 K having a consistent population of 0.23/3 each.

The refined coefficients are 4.15(3) μ_B along the $[1\bar{1}\bar{1}]$ direction and a canting of 1.23(6) μ_B along the [110] direction (see Table I) and equivalently for the other domains. It has to be noted that the model without canting yields $R_F = 12.7\%$, while a nonzero canting improves the fit to $R_F = 9.1\%$ confirming the presence of the YK phase (see Fig. 7 for the corresponding I_{obs} versus I_{cal} plot).

It is commonly expected that increasing flexibility by introducing more fit parameters enhances the quality of the fit. Hence, to assess the significance of the obtained canting at 1.6 K, we analyzed our data utilizing a canted model featuring twelve domains using the 12 K dataset. The result revealed a magnetic moment of 3.75(3) μ_B along the space diagonal and a canting of 0.2(3) μ_B along [110], indicating an insignificant canting. However, analyzing the 1.6 K data using only the

TABLE I. Details of magnetic-structure refinements for different fields at 1.6 K.

$\mu_0 H$ (T)	$\mu_{Mn}\|\|\langle 111\rangle$ (μ_B)	$\mu_{Mn}\|\|\langle 110\rangle$ (μ_B)	$\mu_{Cr}\|\|\langle 111\rangle$ (μ_B)	R_F (%)
0	4.15(3)	1.23(6)	–2.66(2)	9.06
3	3.69(6)	1.87(7)	–2.52(2)	10.67
6	3.36(5)	2.28(6)	–2.54(3)	9.24

four magnetic domains obtained at 12 K, with a canting along [110], yielded similar results: a canting of 1.12(6) μ_B and $R_F = 9.2\%$. This similarity arises because the four roughly equally populated magnetic domains provide sufficiently averaged intensity for each measured (hkl) reflection, which is not significantly altered with the addition of more domains. Nevertheless, it is crucial that the twelve-domain model produces a convincing fit, as this scenario aligns best with the group-subgroup relationship between different symmetries.

B. Neutron diffraction up to 6 T

1. *Temperature and field dependence of characteristic reflections*

Figure 8(a) displays the temperature dependence of the (200) reflection measured at ZF and 6 T. Notably, in contrast to the ZF data, where $T_{YK} \approx 5$ K, the 6 T data shows a shift of T_{YK} towards higher temperature (≈8.5 K). This aligns with the observations made using bulk-measurement techniques [21,24]. Additionally, below T_{YK}, the reflection intensity is stronger for the 6 T data, suggesting an enhanced Mn1-Mn2 canting angle in the presence of a magnetic field [see Fig. S2 within the Supplemental Material [12] for temperature dependence of $(2\bar{2}0)$ and $(11\bar{3})$ at 0 and 6 T]. Figures 8(b) and 8(c) illustrate the field dependence of the (200) and $(11\bar{3})$ reflections at 1.6 K, respectively. Both reflections exhibit a gradual intensity increase with rising field, without any sharp transitions observed up to 6 T. While the magnetic structure evolves gradually with increasing field from zero, no hysteresis is detected between up- and down-field sweeps.

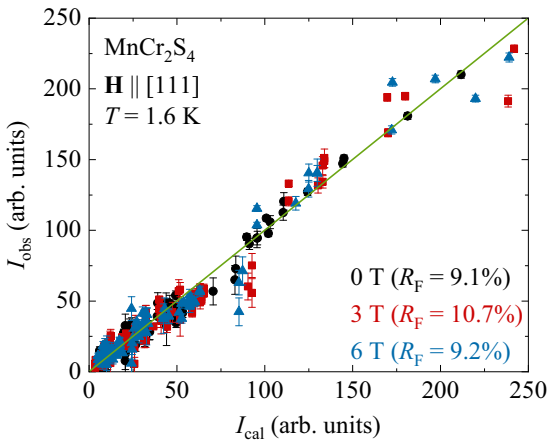

FIG. 7. Observed vs calculated intensity plot for 0, 3, and 6 T data measured at 1.6 K (D23, CEA-CRG, ILL).

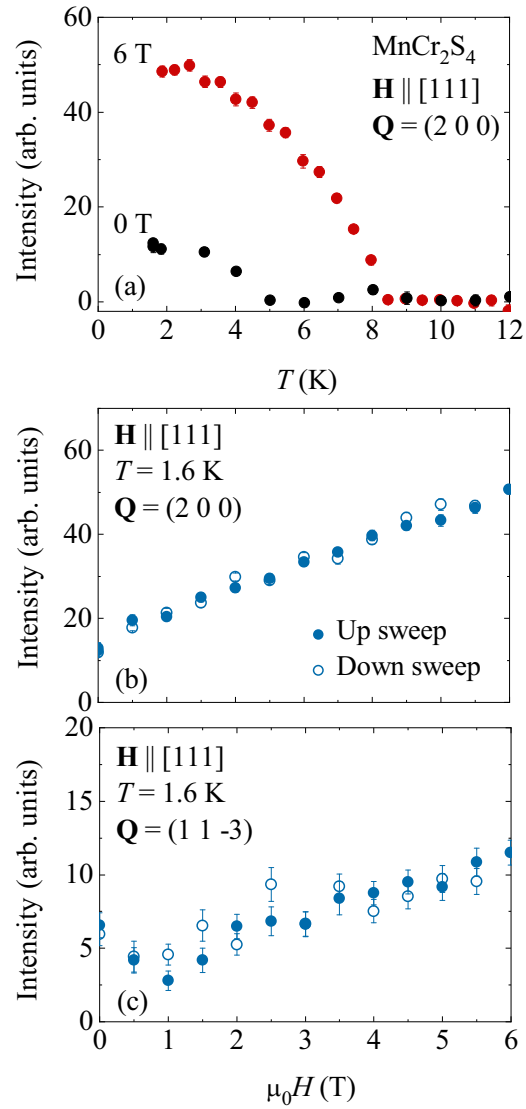

FIG. 8. (a) Temperature dependence of the (200) reflection measured in zero field and 6 T. [(b),(c)] Magnetic-field dependence at 1.6 K of the (200) and $(11\bar{3})$ reflections up to 6 T (D23, CEA-CRG, ILL).

2. *Magnetic structure at 1.6 K for $\mu_0 H = 3$ T and 6 T*

To derive the magnetic structure at low fields, the same strategy for data selection as for ZF was implemented for the in-field data. Specifically, the 80 K ZF data were subtracted from the in-field 1.6 K datasets to obtain the (hkl) lists containing purely magnetic contributions.

The same model for the magnetic structure was applied to the 3 and 6 T datasets as for the ZF dataset. Initially, a fixed domain population was maintained, resulting in a noticeable increase in the canting component and a simultaneous increase in the moment along ⟨111⟩ for the Cr site. However, the fit quality deteriorated significantly compared to the ZF refinement, evident in clear deviations from the observed versus calculated intensities for certain groups of reflections. Subsequently, in a second refinement step, the population of domain groups corresponding to different ⟨111⟩ directions was adjusted. This refinement revealed a distinct

TABLE II. Comparison of magnetic structures at 6 T for different temperatures.

T (K)	$\mu_{Mn}\|\|\langle 111\rangle$ (μ_B)	$\mu_{Mn}\|\|\langle 110\rangle$ (μ_B)	$\mu_{Cr}\|\|\langle 111\rangle$ (μ_B)	R_F (%)
1.6	3.36(5)	2.28(6)	–2.54(3)	9.24
12	3.00(6)	0.3(3)	–2.50(3)	12.6
50	1.58(5)	–0.22(25)	–2.18(2)	14.49

selection of the [111] domains, prompting a third step in which only the domains 10 to 12 (Fig. 6) were used. It is worth noting that in the second and third refinement steps, the Cr moment approached the ZF value, suggesting that the initial increase observed in the first refinement step compensated for an incorrect domain distribution. Interestingly, in the three-domain refinement, only two of them are populated, with one being favored at the expense of the other. This might be because of imperfect sample orientation with respect to the field direction. Figure 7 illustrates the fit quality of our refinements through I_{cal} versus I_{obs} plots. Table I outlines the magnetic field dependencies of the 1.6 K magnetic structure. As is evident, with rising field, Mn canting increases, whereas the Cr moment remains practically insensitive to the field.

3. Magnetic structure at 12 K and 50 K for $\mu_0 H = 6$ T

The data collected within the temperature range $T_{YK} \leqslant T \leqslant T_{FiM}$ shed light on the influence of magnetic fields on the FiM configuration. Based on the model established at 1.6 K and 6 T and using the same refinement approach as previously, we observed a selection of the [111] domains. However, at 12 and 50 K, the refinements yielded values for the component describing the canting of Mn spins along the $\langle 110\rangle$ direction that were small and comparable to the error margins, indicating an absence of significant canting. Consequently, the domains 10 to 12 became indistinguishable, resulting in a diverging fit. Indeed, under these conditions, the data can be adequately explained by a single domain. A comparison of the refinement results at 6 T for various temperatures is presented in Table II. As shown, at low field, with increasing temperature above T_{YK}, the YK phase is replaced by a FiM structure, which persists up to at least 50 K.

C. Neutron diffraction in static magnetic fields up to 25.9 T

Figure 9 (top panel) shows the field dependence up to 25.9 T of the integrated intensities of $(0\bar{2}0)$, $(1\bar{3}1)$, and $(2\bar{2}0)$ for field applied along the [111] direction at $T = 1.6$ K. At around 11 T, both $(0\bar{2}0)$ and $(1\bar{3}1)$ exhibit a sharp increase, indicating the $\mu_0 H_1$ phase boundary. As the field continues to increase up to 25.9 T, these intensities keep rising without any further anomaly. In contrast, the intensity of the $(2\bar{2}0)$ reflection decreases with increasing field and eventually approaches zero. Here, too, a distinct feature is observed around $\mu_0 H_1$.

An important result from the magnetic-structure refinement against the D23 data, which included a sufficiently large number of reflections, was the selection of magnetic domains

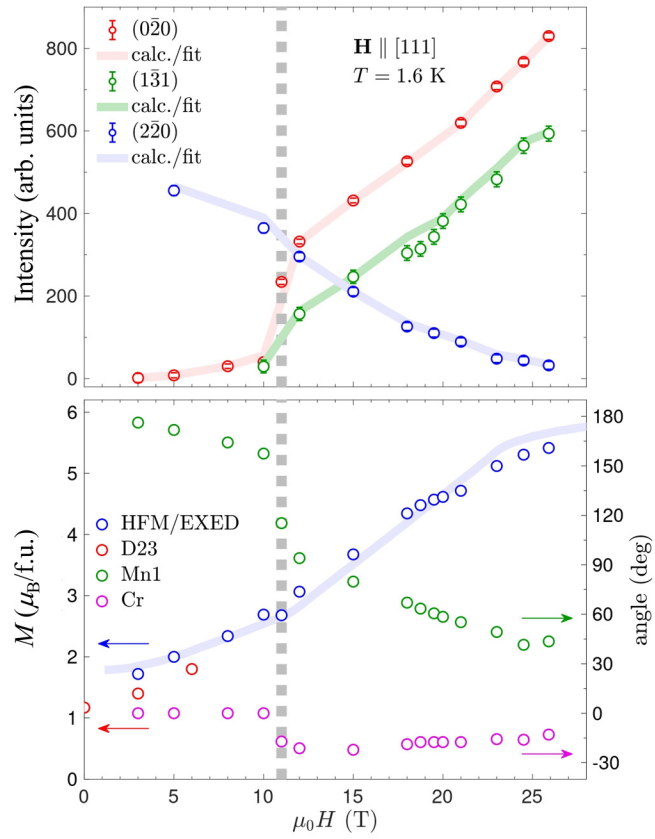

FIG. 9. (Top) Magnetic-field-dependent integrated intensities of the $(0\bar{2}0)$, $(1\bar{3}1)$, and $(2\bar{2}0)$ reflections (open circles) measured at 1.6 K and for field applied along [111] (HFM/EXED instrument, HZB). The solid lines represent the calculated integrated intensities of the same reflections. (Bottom) Comparison between the measured magnetization data reported in Ref. [29] (blue line) with our calculated values (blue/red circles) derived from the spin-model refinements. In addition, the green and pink circles indicate, respectively, the field dependence of the Mn1 and Cr canting angles with respect to the $\langle 111\rangle$ direction. The dotted line delineates the phase transition at $\mu_0 H_1$.

with the [111] axis along the field. Therefore, for the analysis of the HFM/EXED data, and considering further symmetry breaking in the intermediate phase between 11 and 25.9 T, we used the six magnetic domains keeping the [111] direction invariant. They were assumed to have equal populations because of the lack of specific information. The corresponding symmetry operators relating the magnetic domains are:

(1) x y z
(2) z x y
(3) y z x
(4) –x+1/4 –y+1/4 –z+1/4
(5) –y+1/4 –z+1/4 –x+1/4
(6) –z+1/4 –x+1/4 –y+1/4

Since the HFM/EXED instrument was specifically optimized for high-field experiments, we used information from our D23 analysis as starting point to account for the low-field data ($\leqslant 6$ T). This analysis revealed a small but finite YK-type canting between the Mn1 and Mn2 spins in ZF below T_{YK}, with the canting angle increasing with field up to

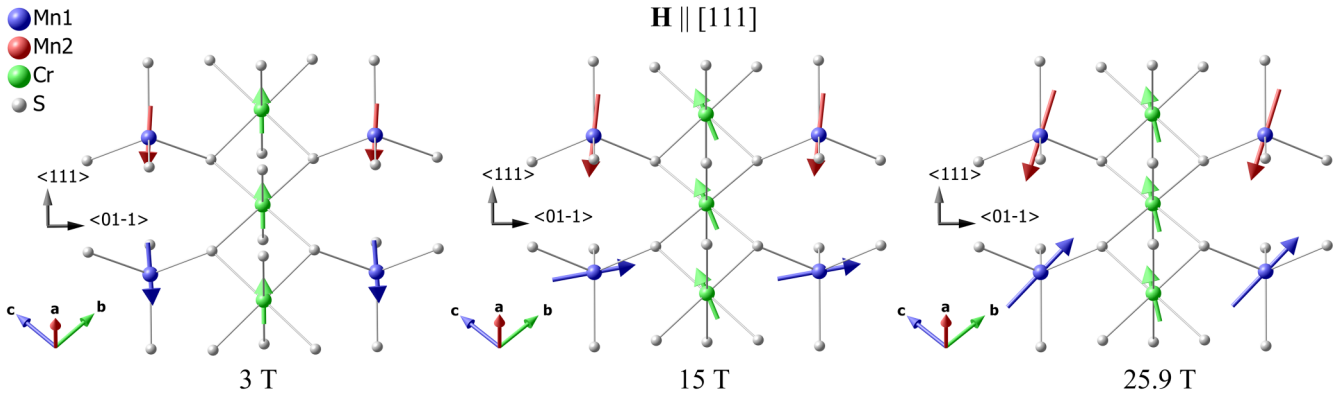

FIG. 10. Overview of a representative domain refined at 1.6 K for fields applied along the ⟨111⟩ direction, showing the increasing canting angle between Mn1 and Mn2 along the $\langle 01\bar{1}\rangle$ direction with rising field. The figure also illustrates the small deviation of the Cr spins from the ⟨111⟩ direction above $\mu_0 H_1 \approx 11$ T.

6 T. To identify a suitable spin-structure model that explains our HFM/EXED results up to 25.9 T, the primary degree of freedom considered was the rotation of one Mn spin from the canted position towards a parallel alignment with the field direction [24,25,29]. During our experiment, the integrated intensities of the $(0\bar{2}0)$, $(1\bar{3}1)$, and $(2\bar{2}0)$ reflections were not all recorded at exactly the same field values. Therefore, at field values with three observations, up to two parameters were refined at a time, whereas at field values with one or two observations, the spin coefficients were set to interpolated values. While aligning our calculations with the observed intensities, we ensured that the magnetization deduced from neutron data closely matched the reported bulk data [29]. In a subsequent refinement step, we adjusted a second coefficient to incorporate a small deviation of the Cr moments from the applied field direction, based on the Cr-spin configuration proposed in Refs [25,26,29]. At this stage, the total moment of Mn1 was constrained to be equal to the total moment of Mn2 for all field values. Additionally, the Cr tilt angles obtained from our mean-field analysis, discussed below, were used as initial values to complete the refinement successfully. As an example, Fig. 10 illustrates a domain refined at 1.6 K for three field values (3, 15, and 25.9 T), showing the Mn canting along the $\langle 01\bar{1}\rangle$ direction and its increase with field, as well as the deviation of the Cr spins from the ⟨111⟩ direction at 15 and 25.9 T in the intermediate phase.

The calculated integrated intensities of the $(0\bar{2}0)$ and $(2\bar{2}0)$ reflections, as a function of magnetic field, are in excellent agreement with the measured ones (top panel of Fig. 9). The integrated intensities of the $(1\bar{3}1)$ reflection are slightly overestimated between 15 and 20 T. This discrepancy is likely caused by the larger error bars associated with this reflection, which led us to assign more weight to the $(0\bar{2}0)$ and $(2\bar{2}0)$ reflections in the refinement algorithm. The calculated magnetization (blue and red circles in the bottom panel of Fig. 9) also aligns well with the experimental data reported by Yamamoto *et al.* (blue line) [29]. The rotation angle of the Mn1 spin with respect to the ⟨111⟩ direction (green circles in the bottom panel of Fig. 9) shows a sharp jump at the phase boundary $\mu_0 H_1$, whereas the Cr spins deviate slightly from the field direction, displaying a tilt angle of about 20° at 15 T, which then gradually decreases. The nonzero angles for both spin orientations up to 25.9 T suggest that the compound has not yet entered the antiferromagnetic phase above $\mu_0 H_2$.

The refined magnetic moments derived from the D23 data yield magnetization values that are slightly lower than the macroscopic ones (red circles in Fig. 9, bottom panel). However, the calculated magnetization from our HFM/EXED data refinement fits perfectly to the measured ones. By that, we demonstrate that our magnetic structure model for the intermediate state between 11 and 25.9 T is consistent with the measured reflection intensities and magnetization. Additionally, it confirms the asymmetric spin configuration proposed previously by Miyata *et al.* and Yamamoto *et al.* [25,29]. As the magnetic field increases above $\mu_0 H_1$, one Mn spin rotates from its canted position towards a parallel alignment with the field, while the other remains nearly antiparallel. Meanwhile, the Cr spins tilt lightly before gradually realigning parallel to the field beyond $\mu_0 H_2$. The observation that only one Mn moment starts to align with the field between $\mu_0 H_1$ and $\mu_0 H_2$ results from spin-energy minimization in the presence of the applied magnetic field. The inequivalence of the Mn moments, combined with the nature of the exchange interactions and the Zeeman effect, leads to a configuration where one Mn moment progressively aligns with the field while the other does not, thus minimizing the system's total energy.

D. Neutron diffraction in pulsed magnetic fields up to 35 T

As an extension of our neutron experiments in static fields, we performed pulsed-field SCND measurements to gain additional insight into the spin-structure evolution between $\mu_0 H_2$ (≈25 T) and $\mu_0 H_3$ (≈50 T). In this field regime, a robust magnetization plateau appears, which is attributed to strong spin-lattice coupling [24,25]. More than 200 magnetic field pulses were accumulated in fields up to 35 T at 2 K to investigate the field dependence of the diffracted intensity of the (002) reflection. The resulting data is shown in Fig. 11. Notably, a distinct flat region emerges for fields exceeding approximately 26 T, resembling the high-field magnetization data [24,25], thereby delineating the $\mu_0 H_2$ phase boundary. Subsequent measurements were performed at temperatures of 9, 12.5, and 18 K, each accumulating data of over 130

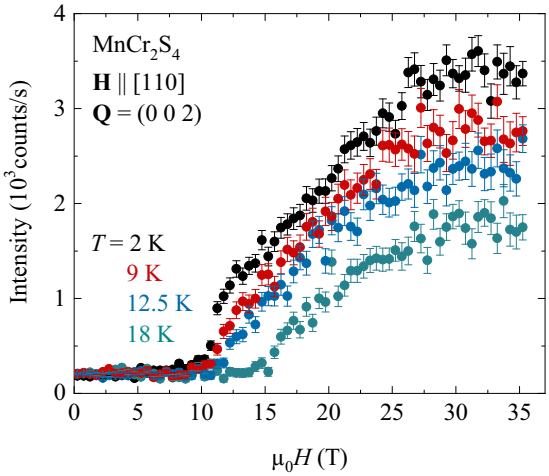

FIG. 11. Magnetic field dependence of the peak intensity of the (002) reflection measured at four different temperatures in pulsed fields up to 35 T (only data for decreasing field are shown for clarity; see Fig. S4 within the Supplemental Material [12] for data collected during rising field) (IN22, CEA-CRG, ILL).

magnetic pulses. As illustrated in Fig. 11, up to 18 K the onset of the plateau region, indicating the phase boundary at $\mu_0 H_2$, is rather insensitive to temperature. The phase boundary at $\mu_0 H_1$ remains relatively constant at approximately 11 T up to 12.5 K, but shifts to around 15 T at 18 K.

As the magnetic field was applied this time along the [110] direction, we selected the eight magnetic domains that preserve a tilt along the $[01\bar{1}]$ direction to determine the magnetic structures. It is important to note that this selection among all potential ⟨110⟩ directions was made to maintain consistency with our previous analysis of HFM/EXED data and to minimize potential confusion. Consequently, this selection includes domains with distinct ⟨111⟩ spin orientations, as follows:

(1) x y z
(2) x+1/2 –y –z+1/2
(3) –x+3/4 z+3/4 y+1/4
(4) –x+1/4 –z+1/4 –y+1/4
(5) –x+1/4 –y+1/4 –z+1/4
(6) –x+3/4 y+1/4 z+3/4
(7) x+1/2 –z+1/2 –y
(8) x z y

The collinear spin-structure model, enabling us to reproduce the experimentally observed bulk magnetization of 6 μ_B, was employed to adjust the scale factor to match the IN22 intensities at the maximum field. The counts at the lowest field were considered as the background (∼185 counts/s) and added to the calculated intensities derived from the models in MAG2POL. Consistently, the same structure was used at 27 T to build the plateau. The top panel of Fig. 12 shows the remarkable agreement between the experimental and calculated intensities of the (002) reflection at 2 K. In the low-field phase ($\mu_0 H < 11$ T), the YK canting was adjusted, while in the intermediate phase (11 T $< \mu_0 H <$ 27 T), the asymmetric models derived from the HFM/EXED data analysis were employed. Calculating six points along the curve was sufficient to describe it accurately. Importantly, our models ensure a

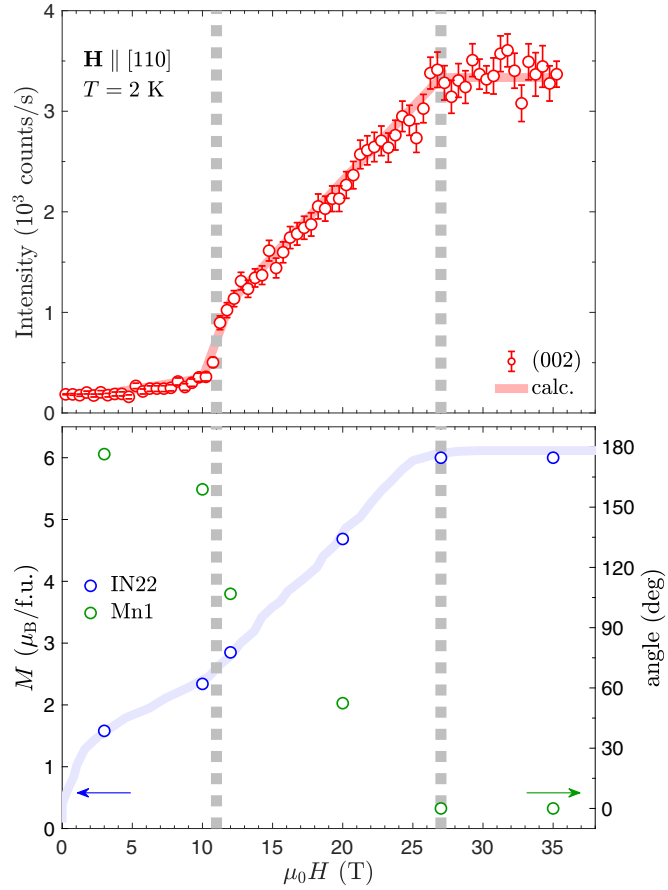

FIG. 12. (Top) Magnetic-field-dependent intensity of the (002) reflection (open circles) measured at $T = 2$ K (IN22, ILL). The solid line represents the calculated intensity of the same reflection using the spin arrangement proposed in the text based on the neutron-data modeling. (Bottom) Comparison between the measured magnetization data reported in reference [25] (blue line) with our calculated values (blue circles) derived from the neutron-data modeling. Additionally, the green circles indicate the field dependence of the Mn1 canting angle with respect to the ⟨110⟩ direction. The dotted lines mark the phase transitions at $\mu_0 H_1$ and $\mu_0 H_2$.

close match between the bulk magnetization (with **H** || ⟨110⟩), adopted from the study by Miyata *et al.* [25] (blue line), and the calculated one (blue circles), as depicted in the bottom panel of Fig. 12. Furthermore, in the same figure, the green circles illustrate that within the plateau region above $\mu_0 H_2$, the Mn1 spins align along the ⟨110⟩ direction, effectively becoming parallel to the Cr spin.

E. Mean-field calculation

Based on the knowledge of magnetic structures obtained from our experimental results and analyses, we constructed a mean-field spin Hamiltonian ($\mathcal{H}_{MF}$) for $MnCr_2S_4$ to estimate the leading magnetic exchange couplings and their field dependencies. As mentioned above, Mn ions form a diamond lattice, and its sublattice symmetry is broken in the field-induced phases, leading to symmetrically inequivalent Mn1 and Mn2 spins. Our determination of the magnetic structure from neutron diffraction data shows that the magnetic inter-

action between the Cr spins is strongly ferromagnetic, while the interactions between the Mn and Cr spins are antiferromagnetic. The mean-field Hamiltonian of the magnetic spinel compound is given by

$$\mathcal{H}_{\rm MF} = 4J_{\rm MM}\boldsymbol{S}_{\rm Mn1}\cdot\boldsymbol{S}_{\rm Mn2}+12(J_{\rm CM1}\boldsymbol{S}_{\rm Mn1}\cdot\boldsymbol{S}_{\rm Cr}+J_{\rm CM2}\boldsymbol{S}_{\rm Mn2}\cdot\boldsymbol{S}_{\rm Cr}) + 12J_{\rm CC}\boldsymbol{S}_{\rm Cr}\cdot\boldsymbol{S}_{\rm Cr}-\boldsymbol{h}\cdot(\boldsymbol{S}_{\rm Mn1}+\boldsymbol{S}_{\rm Mn2}+4\boldsymbol{S}_{\rm Cr}), \quad (1)$$

where $J_{\rm MM}$, $J_{\rm CM1}$, $J_{\rm CM2}$, and $J_{\rm CC}$ denote the exchange couplings between Mn1 and Mn2, Cr and Mn1, Cr and Mn2, and Cr atoms, respectively, and $\boldsymbol{h}$ is the magnetic field.

Here, we assume that the spins form a coplanar state and parametrize the spin structure by defining angles $\theta_{\rm Mn1}$, $\theta_{\rm Mn2}$, and $\theta_{\rm Cr}$ measured from the magnetic field direction ($-\pi \leqslant \theta_{\rm Mn1}, \theta_{\rm Mn2}, \theta_{\rm Cr} < \pi$). In this parametrization, the Hamiltonian can be written in the following simple form:

$$\begin{aligned}\mathcal{H}_{\rm MF} &= 4J_{\rm MM}S_{\rm Mn1}S_{\rm Mn2}\cos(\theta_{\rm Mn2}-\theta_{\rm Mn1})\\ &+ 12J_{\rm CM1}S_{\rm Mn1}S_{\rm Cr}\cos(\theta_{\rm Mn1}-\theta_{\rm Cr})\\ &+ 12J_{\rm CM2}S_{\rm Mn2}S_{\rm Cr}\cos(\theta_{\rm Mn2}-\theta_{\rm Cr})+12J_{\rm CC}S_{\rm Cr}^2\\ &- h(S_{\rm Mn1}\cos\theta_{\rm Mn1}+S_{\rm Mn2}\cos\theta_{\rm Mn2}+4S_{\rm Cr}\cos\theta_{\rm Cr}).\end{aligned} \quad (2)$$

The energy is minimized by the optimal angles, which leads to the following equations:

$$\begin{aligned}\frac{\partial\mathcal{H}_{\rm MF}}{\partial\theta_{\rm Mn1}} &= 4J_{\rm MM}S_{\rm Mn1}S_{\rm Mn2}\sin(\theta_{\rm Mn2}-\theta_{\rm Mn1})\\ &- 12J_{\rm CM1}S_{\rm Mn1}S_{\rm Cr}\sin(\theta_{\rm Mn1}-\theta_{\rm Cr})\\ &+ hS_{\rm Mn1}\sin\theta_{\rm Mn1}=0,\end{aligned} \quad (3)$$

$$\begin{aligned}\frac{\partial\mathcal{H}_{\rm MF}}{\partial\theta_{\rm Mn2}} &= -4J_{\rm MM}S_{\rm Mn1}S_{\rm Mn2}\sin(\theta_{\rm Mn2}-\theta_{\rm Mn1})\\ &- 12J_{\rm CM2}S_{\rm Mn2}S_{\rm Cr}\sin(\theta_{\rm Mn2}-\theta_{\rm Cr})\\ &+ hS_{\rm Mn2}\sin\theta_{\rm Mn2}=0,\end{aligned} \quad (4)$$

$$\begin{aligned}\frac{\partial\mathcal{H}_{\rm MF}}{\partial\theta_{\rm Cr}} &= 12(J_{\rm CM1}S_{\rm Mn1}S_{\rm Cr}\sin(\theta_{\rm Mn1}-\theta_{\rm Cr})\\ &+ 12J_{\rm CM2}S_{\rm Mn2}S_{\rm Cr}\sin(\theta_{\rm Mn2}-\theta_{\rm Cr})\\ &+ 4hS_{\rm Cr}\sin\theta_{\rm Cr}=0.\end{aligned} \quad (5)$$

By adding Eqs. (3), (4), and (5), we obtain

$$S_{\rm Mn1}\sin\theta_{\rm Mn1}+S_{\rm Mn2}\sin\theta_{\rm Mn2}+4S_{\rm Cr}\sin\theta_{\rm Cr}=0 \quad (6)$$

for the mean-field solution. Notably, the experimentally obtained value of $S_{\rm Mn1}\sin\theta_{\rm Mn1}+S_{\rm Mn2}\sin\theta_{\rm Mn2}+4S_{\rm Cr}\sin\theta_{\rm Cr}\equiv\Delta_{MF}$ quantifies how much the spin structure deviates from the mean-field solution.

If we assume a perfect YK-type structure, that is,

$$\theta_{\rm Cr}=0, \quad (7)$$

$$\theta_{\rm Mn1}+\theta_{\rm Mn2}=0, \quad (8)$$

$$S_{\rm Mn1}=S_{\rm Mn2}\equiv S_{\rm Mn}, \quad (9)$$

the Hamiltonian (2) reduces to

$$\begin{aligned}\mathcal{H}_{\rm MF} &= 4J_{\rm MM}S_{\rm Mn}^2\cos 2\theta_{\rm Mn1}+24J_{\rm CM}S_{\rm Mn}S_{\rm Cr}\cos\theta_{\rm Mn1}\\ &+ 12J_{\rm CC}S_{\rm Cr}^2-h(2S_{\rm Mn}\cos\theta_{\rm Mn1}+4S_{\rm Cr}).\end{aligned} \quad (10)$$

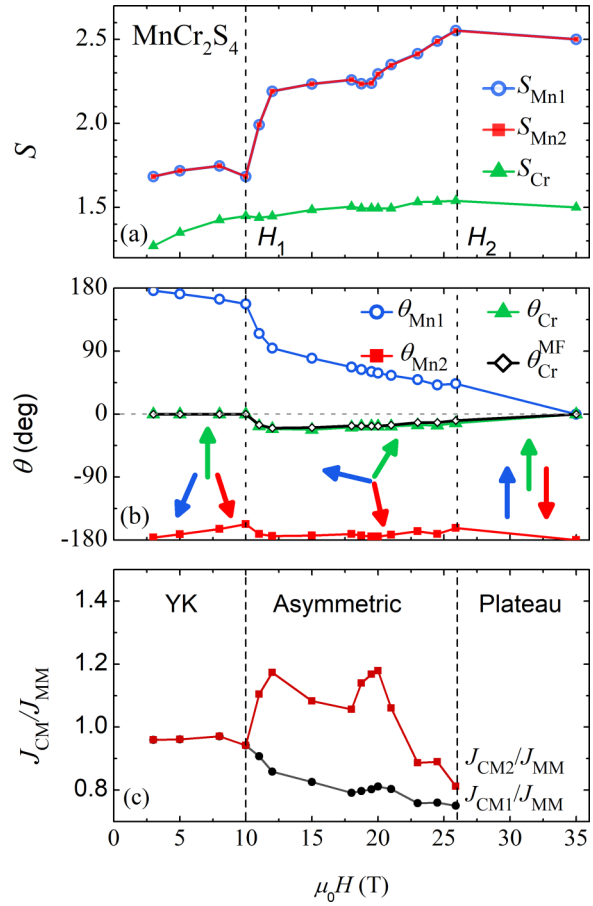

FIG. 13. (a) Magnetic field dependence of the spin value for each magnetic ion, as determined from our neutron-diffraction data. (b) Angle of each spin from the magnetic field direction in the coplanar spin structure. The angles $\theta_{\rm Mn1}$, $\theta_{\rm Mn2}$, and $\theta_{\rm Cr}$ are parameters obtained from our experimental-data refinements, while $\theta_{\rm Cr}^{\rm MF}$ indicates the Cr-spin angle calculated from the mean-field solution obtained using Eq. (6) with all other quantities fixed at their values obtained from our experimental-data analyses. Illustrations of the spin configurations formed by Cr, Mn1, and Mn2 (green, blue, and red arrows, respectively) are shown for the Yafet-Kittel (YK), asymmetric, and plateau phases. (c) Estimated coupling ratio: $J_{\rm CM1}/J_{\rm MM}$ and $J_{\rm CM2}/J_{\rm MM}$. The dotted lines define the theoretical transitions at μ_0H_1 and μ_0H_2.

The energy minimization leads to the following equation:

$$\begin{aligned}\frac{\partial\mathcal{H}_{\rm MF}}{\partial\theta_{\rm Mn1}} &= 2S_{\rm Mn}\sin\theta_{\rm Mn1}(-8J_{\rm MM}S_{\rm Mn}\cos\theta_{\rm Mn1}\\ &- 12J_{\rm CM}S_{\rm Cr}+h)=0.\end{aligned} \quad (11)$$

Thus, for $\sin\theta_{\rm Mn1}\neq 0$,

$$-8J_{\rm MM}S_{\rm Mn}\cos\theta_{\rm Mn1}-12J_{\rm CM}S_{\rm Cr}+h=0. \quad (12)$$

Figure 13(a) shows the spin value S of each ion, as determined by our neutron-data analyses, which are discussed in detail in the earlier sections. The Cr-spin value is close to 3/2, in particular above μ_0H_1, indicating that fluctuations from the fully ferromagnetically ordered state are small. The Mn-spin value is significantly less than 5/2 in the low-field phases, especially in the YK phase, but reaching $S=5/2$ at

the upper end of the plateau phase (at about 26 T). The reduction in effective magnetic moment is expected to be caused by enhanced charge fluctuations, which may contribute to the electric polarization [21]. Note that the Mn-spin values in the two sublattices are identical within error bars. Figure 13(b) shows the angle of each spin from the magnetic field direction in the coplanar structure.

An important consequence of our mean-field analysis is that the Cr-spin angle must be nonzero to satisfy Eq. (6), when the sublattice symmetry of the Mn spins is broken. This is the case between 10 and 26 T, as shown in Fig. 13(b), consistent with the asymmetric (intermediate) phase. Since the Cr-spin angle is more difficult to determine from the experimental data than other quantities, as discussed above, we also calculate the Cr-spin angle of the perfect mean-field solution satisfying Eq. (6), while fixing the other quantities to the values obtained from our neutron-data analyses. The difference between the experimentally obtained angle $\theta_{\rm Cr}$ and the mean-field angle of the Cr spins $\theta_{\rm Cr}^{\rm MF}$ is less than 4° over the measured magnetic fields. Additionally, we obtained $|\Delta_{\rm MF}|/S_{\rm Mn} \sim 0.1$, validating our mean-field analysis.

Using Eqs. (3)–(5), (12), and the experimentally determined spin structure, we estimate the exchange coupling ratio, as plotted in Fig. 13(c). The coupling ratio $J_{\rm CM}/J_{\rm MM}$ is close to 1 in the YK phase, as expected. An estimation of the ratio is not allowed at 35 T, for which all spins are almost parallel to the magnetic field and $\sin\theta_{\rm Mn} = 0$. The two exchange couplings $J_{\rm CM1}$ and $J_{\rm CM2}$ are significantly different between 10 and 26 T in the intermediate phase.

Let us focus here on the Mn spins of the system, which form a diamond lattice. The magnetic interaction with the Cr spins introduces an effective magnetic field acting on the Mn spins. The inequality between $J_{\rm CM1}$ and $J_{\rm CM2}$ produces an effective staggered field $\boldsymbol{h}^{\rm stag}$ at the Mn2 sites and $-\boldsymbol{h}^{\rm stag}$ at the Mn1 sites, where $\boldsymbol{h}^{\rm stag} = \frac{1}{2}(J_{\rm CM2} - J_{\rm CM1})\boldsymbol{S}_{\rm Cr}$. Because of the Cr-spin canting in the intermediate phase, the staggered field has components parallel and perpendicular to the external field. A renormalization group study of the O(N) model [30] shows that the Heisenberg spin system with three spin degrees of freedom ($N = 3$) in a bipartite lattice does not have an asymmetric phase with both longitudinal and transverse ordering simultaneously if the staggered field only has a parallel or perpendicular component. Therefore, the existence of *both components* generated by Cr-canted spins is essential to stabilize the asymmetric phase and the tetracritical point [29].

Our mean-field analysis reveals an extraordinary dependence of the exchange couplings on the magnetic field. The change in the coupling ratio $J_{\rm CM2}/J_{\rm CM1}$ is nonmonotonic and as large as nearly 50%, as shown in Fig. 13(c), being a unique feature of $MnCr_2S_4$. This significant variation appears to be caused by spin-lattice coupling, as evidenced by ultrasound measurements [24,25,29]. Qualitative agreement with the experimentally observed magnetization process was reported in previous calculations using a simple spin-lattice model with bond phonons [25]. However, the simple spin-lattice model with optimized parameters only produces a 20% change in the exchange-coupling ratio in magnetic field. The quantitative deviation from our experimental results is expected to be because of the fact that many phonon modes can couple to the magnetic moments of spinel compounds and that bond phonons do not account for adequate contributions from the lattice degrees of freedom. Obtaining quantitative agreement with experiments is also a major challenge for other magnetic spinel materials [43]. The estimated nonmonotonic change of nearly 50% in the exchange-coupling ratio implies that a more complex spin-lattice model [44] will likely be required for a quantitative comparison with experiments.

IV. SUMMARY AND CONCLUSIONS

Our comprehensive neutron-diffraction study has enabled us to precisely determine the spin configurations in the frustrated spinel compound $MnCr_2S_4$ on a microscopic level.

The refinement of our ZF data below $T_{\rm FiM} \approx 65$ K not only confirms the FiM order with antiparallel alignment of Cr and Mn spins along the ⟨111⟩ direction but also provides direct evidence of the YK phase, discussed nearly 60 years ago by Lotgering, in $MnCr_2S_4$. As the temperature decreases below $T_{\rm YK} \approx 5$ K, the FiM structure is indeed disrupted. Specifically, the Mn1 and Mn2 spins exhibit a small angular deviation from the ⟨111⟩ direction, while the Cr sublattice retains its alignment along ⟨111⟩. This symmetric canting observed under ZF conditions, is a definitive signature of the YK-type magnetic ground state in $MnCr_2S_4$.

Furthermore, as the magnetic field approaches $\mu_0 H_1$, the YK-type magnetic structure becomes more pronounced, evidenced by a gradual increase of the canting angle of the Mn1 and Mn2 spins. However, beyond $\mu_0 H_1$, this symmetric YK-type canted structure disappears, as one of the Mn spins begins to rotate from the canted position towards an alignment parallel to the field, while the Cr spins deviate slightly from the field direction, leading to an asymmetric phase between $\mu_0 H_1$ and $\mu_0 H_2$.

The rotation of the Mn spins finally completes upon crossing $\mu_0 H_2$ and entering the plateau phase between $\mu_0 H_2$ and $\mu_0 H_3$. In this phase, one Mn spin, along with the Cr spins, aligns parallel to the applied field, while the other Mn spin stays nearly antiparallel.

Our mean-field calculations estimate the ratio of AFM Cr-Mn ($J_{\rm CM}$) and Mn-Mn ($J_{\rm MM}$) couplings and their field dependencies, offering further insights into the field-driven transitions in $MnCr_2S_4$. Below $\mu_0 H_1$, $J_{\rm CM}/J_{\rm MM}$ remains close to 1, favoring the stabilization of the YK phase in the presence of strong FM Cr-Cr ($J_{\rm CC}$) coupling. However, above $\mu_0 H_1$, the coupling ratio exhibits a nonmonotonic change, with deviations reaching nearly 50%. This behavior suggests the involvement of intricate spin-lattice coupling mechanisms.

Future efforts could focus on developing a more detailed model to quantitatively understand the complex spin-lattice coupling inherent to this exotic material.

ACKNOWLEDGMENTS

We acknowledge S. Gerisher, R. Wahle, S. Kempfer, P. Heller, and P. Smeibidl from the HFM/EXED team at the HZB for their technical assistance for the use of the 26 T magnet. We thank X. Tonon and E. Lelièvre-Berna from the Services for Advanced Neutron Environments at the Institut Laue-Langevin for their active support with the cryogenics of the 40-T pulsed cryomagnet. This work has been

partly supported by the Deutsche Forschungsgemeinschaft (DFG) through SFB 1143 (Project No. 247310070) and the Würzburg-Dresden Cluster of Excellence on Complexity and Topology in Quantum Matter–*ct.qmat* (EXC 2147, Project Id 39085490). We acknowledge the support of the HLD at HZDR and of the LNCMI-CNRS, both members of the European Magnetic Field Laboratory (EMFL), as well as the support of V.T. via the Project ANCD 20.80009.5007.19 (Moldova). H.S. acknowledges support from JSPS KAKENHI Grants No. JP22K03508 and No. JP24H01609.

[1] R. Moessner and A. P. Ramirez, Geometrical frustration, Phys. Today **59**, 24 (2006).

[2] C. Lacroix, P. Mendels, and F. Mila, *Introduction to Frustrated Magnetism: Materials, Experiments, Theory*, Springer Series in Solid-State Sciences (Springer, Berlin, 2011)

[3] H. T. Diep, *Frustrated Spin Systems*, 2nd ed. (World Scientific, Singapore, 2013).

[4] V. Tsurkan, H.-A. Krug von Nidda, J. Deisenhofer, P. Lunkenheimer, and A. Loidl, On the complexity of spinels: Magnetic, electronic, and polar ground states, Phys. Rep. **926**, 1 (2021).

[5] S. Gao, O. Zaharko, V. Tsurkan, Y. Su, J. S. White, G. Tucker, B. Roessli, F. Bourdarot, R. Sibille, D. Chernyshov *et al.*, Spiral spin-liquid and the emergence of a vortex-like state in $MnSc_2S_4$, Nat. Phys. **13**, 157 (2017).

[6] A. Sundaresan and N. V. Ter-Oganessian, Magnetoelectric and multiferroic properties of spinels, J. Appl. Phys. **129**, 060901 (2021).

[7] J.-H. Chung, M. Matsuda, S.-H. Lee, K. Kakurai, H. Ueda, T. J. Sato, H. Takagi, K.-P. Hong, and S. Park, Statics and dynamics of incommensurate spin order in a geometrically frustrated antiferromagnet $CdCr_2O_4$, Phys. Rev. Lett. **95**, 247204 (2005).

[8] J. E. Greedan, Geometrically frustrated magnetic materials, J. Mater. Chem. **11**, 37 (2001).

[9] B. D. Gaulin and J. S. Gardner, *Experimental studies of pyrochlore antiferromagnets*, in Introduction to Frustrated Magnetism: Materials, Experiments, Theory, edited by C. Lacroix, P. Mendels, and F. Mila (Springer, Berlin, 2011), pp. 177–206.

[10] S. Diaz, S. de Brion, G. Chouteau, B. Canals, V. Simonet, and P. Strobel, Magnetic frustration in the spinel compounds $GeCo_2O_4$ and $GeNi_2O_4$, Phys. Rev. B **74**, 092404 (2006).

[11] X. Fabrèges, E. Ressouche, F. Duc, S. de Brion, M. Amara, C. Detlefs, L. Paolasini, E. Suard, L.-P. Regnault, B. Canals, P. Strobel, and V. Simonet, Field-driven magnetostructural transitions in $GeCo_2O_4$, Phys. Rev. B **95**, 014428 (2017).

[12] See Supplemental Material at http://link.aps.org/supplemental/10.1103/PhysRevB.110.214416 for the nuclear structure details and complementary tables and graphs of the experimental data obtained from our neutron diffraction study of $MnCr_2S_4$ and the analysis performed to determine the zero-field and field-induced magnetic structures.

[13] Y. Yafet and C. Kittel, Antiferromagnetic arrangements in ferrites, Phys. Rev. **87**, 290 (1952).

[14] F. Lotgering, On the ferrimagnetism of some sulfides and oxides, Philips Res. Rep. **11**, 190 (1956).

[15] F. Lotgering, Spin canting in $MnCr_2S_4$, J. Phys. Chem. Solids **29**, 2193 (1968).

[16] R. Plumier and M. Sougi, Étude par diffraction des neutrons d'une transition magnetique à basse temperature dans le thiospinelle $MnCr_2S_4$, C. R. Acad. Sci. B - Sci. Phys. **268**, 1549 (1969).

[17] J. Denis, Y. Allain, and R. Plumier, Magnetic behavior of $MnCr_2S_4$ in high magnetic fields, J. Appl. Phys. **41**, 1091 (1970).

[18] R. Plumier, R. Conte, J. Denis, and Mme M. Nauciel-Bloch, Étude de quelques propriétés magnétiques du thiospinelle $MnCr_2S_4$, J. Phys. Colloques **32**, C1 (1971).

[19] R. Plumier and M. Sougi, Neutron diffraction reinvestigation of $MnCr_2S_4$, in *European Powder Diffraction EPDIC 2*, Materials Science Forum (Trans Tech Publications Ltd, 1993), Vol. 133, pp. 523–528.

[20] V. Tsurkan, M. Mücksch, V. Fritsch, J. Hemberger, M. Klemm, S. Klimm, S. Körner, H.-A. Krug von Nidda, D. Samusi, E.-W. Scheidt, A. Loidl, S. Horn, and R. Tidecks, Magnetic, heat capacity, and conductivity studies of ferrimagnetic $MnCr_2S_4$ single crystals, Phys. Rev. B **68**, 134434 (2003).

[21] A. Ruff, Z. Wang, S. Zherlitsyn, J. Wosnitza, S. Krohns, H.-A. Krug von Nidda, P. Lunkenheimer, V. Tsurkan, and A. Loidl, Multiferroic spin-superfluid and spin-supersolid phases in $MnCr_2S_4$, Phys. Rev. B **100**, 014404 (2019).

[22] J. X. Wang, L. Lin, C. Zhang, H. F. Guo, and J.-M. Liu, Experimental observation of ferroelectricity in ferrimagnet $MnCr_2S_4$, Appl. Phys. Lett. **117**, 032903 (2020).

[23] Y. Allain, J. de Gunzbourg, J. P. Krebs, and A. Miedan-Gros, Pulsed field magnetization measurements up to 500 kOe, Rev. Sci. Instrum. **39**, 1360 (1968).

[24] V. Tsurkan, S. Zherlitsyn, L. Prodan, V. Felea, P. T. Cong, Y. Skourski, Z. Wang, J. Deisenhofer, H.-A. Krug von Nidda *et al.*, Ultra-robust high-field magnetization plateau and supersolidity in bond-frustrated $MnCr_2S_4$, Sci. Adv. **3**, e1601982 (2017).

[25] A. Miyata, H. Suwa, T. Nomura, L. Prodan, V. Felea, Y. Skourski, J. Deisenhofer, H.-A. Krug von Nidda, O. Portugall, S. Zherlitsyn, V. Tsurkan, J. Wosnitza, and A. Loidl, Spin-lattice coupling in a ferrimagnetic spinel: Exotic $H - T$ phase diagram of $MnCr_2S_4$ up to 110 T, Phys. Rev. B **101**, 054432 (2020).

[26] R. Plumier, The magnetic-structure of sulfur spinel $MnCr_2S_4$ under applied magnetic-field, J. Phys. Chem. Solids **41**, 871 (1980).

[27] H. Matsuda and T. Tsuneto, Off-diagonal long-range order in solids, Prog. Theor. Phys. Suppl. **46**, 411 (1970).

[28] K.-S. Liu and M. E. Fisher, Quantum lattice gas and the existence of a supersolid, J. Low Temp. Phys. **10**, 655 (1973).

[29] S. Yamamoto, H. Suwa, T. Kihara, T. Nomura, Y. Kotani, T. Nakamura, Y. Skourski, S. Zherlitsyn, L. Prodan, V. Tsurkan, H. Nojiri, A. Loidl, and J. Wosnitza, Element-specific field-induced spin reorientation and tetracritical point in $MnCr_2S_4$, Phys. Rev. B **103**, L020408 (2021).

[30] J. M. Kosterlitz, D. R. Nelson, and M. E. Fisher, Bicritical and tetracritical points in anisotropic antiferromagnetic systems, Phys. Rev. B **13**, 412 (1976).

[31] N. Menyuk, K. Dwight, and A. Wold, Magnetic properties of $MnCr_2S_4$, J. Appl. Phys. **36**, 1088 (1965).

[32] K. Dwight, N. Menyuk, and T. A. Kaplan, Diffuse paramagnetic neutron scattering in chromium spinels, J. Appl. Phys. **36**, 1090 (1965).

[33] H. Schäfer, *Chemische Transportreaktionen: Der Transport anorganischer Stoffe über die Gasphase und seine Anwendungen* (Verlag Chemie, Weinheim, 1962).

[34] O. Prokhnenko, W.-D. Stein, H.-J. Bleif, M. Fromme, M. Bartkowiak, and T. Wilpert, Time-of-flight extreme environment diffractometer at the Helmholtz-Zentrum Berlin, Rev. Sci. Instrum. **86**, 033102 (2015).

[35] P. Smeibidl, M. Bird, H. Ehmler, I. Dixon, J. Heinrich, M. Hoffmann, S. Kempfer, S. Bole, J. Toth, O. Prokhnenko, and B. Lake, First hybrid magnet for neutron scattering at Helmholtz-Zentrum Berlin, IEEE Trans. Appl. Supercond. **26**, 1 (2016).

[36] O. Prokhnenko, P. Smeibidl, W.-D. Stein, M. Bartkowiak, and N. Stüsser, HFM/EXED: The high magnetic field facility for neutron scattering at BER II, J. Large-Scale Res. Facilities JLSRF **3**, A115 (2017).

[37] M. Bartkowiak, K. Prokeš, M. Fromme, A. Budack, J. Dirlick, and O. Prokhnenko, EXEQ and InEXEQ: Software tools for experiment planning at the extreme environment diffractometer, J. Appl. Crystallogr. **53**, 1613 (2020).

[38] O. Arnold, J. C. Bilheux, J. M. Borreguero, A. Buts, S. I. Campbell, L. Chapon, M. Doucet, N. Draper, R. Ferraz Leal, M. A. Gigg *et al.*, Mantid−Data analysis and visualization package for neutron scattering and μSR experiments, Nucl. Instrum. Methods Phys. Res. Sect. A **764**, 156 (2014).

[39] F. Duc, X. Tonon, J. Billette, B. Rollet, W. Knafo, F. Bourdarot, J. Béard, F. Mantegazza, B. Longuet, J. E. Lorenzo *et al.*, 40-Tesla pulsed-field cryomagnet for single crystal neutron diffraction, Rev. Sci. Instrum. **89**, 053905 (2018).

[40] N. Qureshi, *Mag2Pol*: A program for the analysis of spherical neutron polarimetry, flipping ratio and integrated intensity data, J. Appl. Crystallogr. **52**, 175 (2019).

[41] J. Rodríguez-Carvajal, Recent advances in magnetic structure determination by neutron powder diffraction, Phys. B: Condens. Matter **192**, 55 (1993).

[42] G. M. Sheldrick, A short history of SHELX, Acta Crystallogr. A: Found. Crystallogr. **64**, 112 (2008).

[43] A. Miyata, H. Ueda, Y. Ueda, Y. Motome, N. Shannon, K. Penc, and S. Takeyama, Magnetic phases of $ZnCr_2O_4$ revealed by magneto-optical studies under ultra-high magnetic fields of up to 600 T, J. Phys. Soc. Jpn. **81**, 114701 (2012).

[44] M. Gen and H. Suwa, Nematicity and fractional magnetization plateaus induced by spin-lattice coupling in the classical Kagome-lattice Heisenberg antiferromagnet, Phys. Rev. B **105**, 174424 (2022).